Supporting Information

Unlocking Luminescence by Decoupling Quenching Vibrations in $Au_{21}SR_{17}$ Nanocluster: Backbone Flexibility versus Ligand Dynamics

Shuyi He,[1‡] Qiang Ding,[2‡] Yinghao Wu,[3‡] Xiaohan Liu,[1] Longying Li,[1] Xinyi Zhao,[1] Xun Yuan,[3] Liren Liu,[2]* Jishi Chen[1]**

[1]College of Chemistry and Chemical Engineering, Shandong Sino-Japanese Center for Collaborative Research of Carbon Nanomaterials, Qingdao University, Qingdao 266071, P. R. China

[2]Department of Physics, School of Physical and Mathematical Sciences, Nanjing Tech University, Nanjing 210009, Jiangsu, P. R. China

[3]School of Materials Science and Engineering, Qingdao University of Science and Technology, Qingdao 266042, P. R. China

[4]College of Applied Technology, Qingdao University, Qingdao 266071, P. R. China

‡These authors contributed equally: Shuyi He, Qiang Ding, Yinghao Wu

*Corresponding authors. Email: yuanxun@qust.edu.cn; lrliu@njtech.edu.cn; chenjishi@qdu.edu.cn

Experimental Details

Materials and agents Hydrogen tetrachloroaurate(III) tetrahydrate ($HAuCl_4 \cdot 4H_2O$, >99.9% metals basis), sodium hydroxide (NaOH, AR, ≥96.0%), sodium borohydride ($NaBH_4$, 98%), hydrochloric acid (HCl, AR, 37%), glycerol (AR, 99%) toluene (AR, 99.5%) and anhydrous ethanol (EtOH, AR, 99%) were purchased from Sinopharm Chemical Reagent Co., Ltd.; L-Cysteine (Cys, AR, ≥98.5%), L-glutathione (HSG, RG, 99%), and tetraoctylammonium bromide (TOABr, AR, 98%) were purchased from Adamas-beta; Carbon monoxide (CO, 99.9%) was obtained from Qingdao Ludong Air Co., Ltd.. Ultrapure Millipore water (18.2 $M\Omega \cdot cm^{-1}$) was used.

Synthesis of $Au_{21}Cys_{17}$

Under stirring at 500 rpm, the aqueous solution of $HAuCl_4$ (1 mL, 48.56 mM) was introduced into a 100 mL reaction flask with 40 mL aqueous solution of L-cysteine (Cys, 11.8 mg). The initially yellow solution turned milky white. After 5 minutes, the reaction mixture was heated in a 30 °C water bath, and 3 mL 1 M NaOH solution was added. Subsequently, 20 mL of EtOH and 15 μL of $NaBH_4$ (4.3 mg dissolved in 1 mL of 0.2 M NaOH) were added in sequence. The reaction was then allowed to proceed for 3 hours under continuous stirring to yield $Au_{21}Cys_{17}$ nanoclusters.

The crude product was precipitated by adding anhydrous ethanol to the reaction solution at a 2:1 volume ratio. The suspension was then centrifuged at 10,000 rpm for 3 minutes to collect the nanoclusters. The collected precipitate was subsequently was washed three times with ethanol. Following the washes, residual ethanol was removed by lyophilization. The resulting solid was then redissolved in deionized water and transferred to a 3k Da molecular weight cutoff dialysis bag (Viskase). Dialysis was performed at 4 °C for 24 hours to eliminate unreacted precursors and byproducts. After dialysis, the dialysate was treated with 4 volumes of ethanol, followed by centrifugation to collect the precipitate. Finally, the purified product was lyophilized to obtain a final powder. The solid sample was then freeze-dried and stored at -18 °C.

Synthesis of $Au_{22}SG_{18}$

The $Au_{22}SG_{18}$ was synthesized by a CO reduction method adapted from Yu.[S1] In a representative synthesis, aqueous solution of $HAuCl_4$ (1 mL, 48.56 mM) were added to a 100 mL reaction flask containing 49 mL of L-

glutathione (HSG, 11.8 mg) aqueous solution under stirring at 500 rpm. After 5 min, the reaction mixture's pH was adjusted to 11.0 using NaOH solution (1 M). Carbon monoxide (CO) was then bubbled through the solution for 2 minutes, following which the reaction vessel was sealed. Upon 30 minutes of reaction, the pH was reduced to 2.5 by addition of 1 M HCl. The sealed reaction solution was aged for an additional 24 hours, resulting in the formation of an aqueous solution of $Au_{22}SG_{18}$.

Subsequent purification and collection procedures followed an analogous protocol to that described for $Au_{21}Cys_{17}$ in preceding section.

TOABr-mediated phase transfer of $Au_{21}Cys_{17}$ and $Au_{22}SG_{18}$ to toluene

The gold clusters, $Au_{21}Cys_{17}$ or $Au_{22}SG_{18}$ (15 mg), were dissolved in 14 mL of deionized water. The pH of the solution was then adjusted to 12 using 1 M NaOH, followed by the addition of pH 12 aqueous solution to reach a final volume of 15 mL. Subsequently, 5 mL of the cluster-containing aqueous solution was transferred to a reaction flask. A toluene solution containing TOABr (50 mg) was then added, and the mixture was stirred at 500 rpm. Within approximately 30 minutes, the aqueous phase became colorless, while the toluene phase turned a reddish-brown color, as depicted in Figure S7.

Characterization:

The pH value of solution was texted by a SevenCompact S210 desktop pH meter (Mettler Toledo, Switzerland).

UV-vis-NIR spectra were acquired using a UV-2700 spectrophotometer (Shimadzu, Japan). Absorption spectra of the reaction solutions were measured without any concentration or dilution. For powder samples, the material was dissolved in deionized water until completely dissolved before measurement. Time-dependent absorption spectra were recorded by transferring aliquots of the reaction solution into sealed 3.5 mL cuvettes. Before sealing, each aliquot was purged with CO gas for 2 minutes. The sealing process and subsequent placement of the cuvette into the spectrophotometer's sample holder took approximately 1-2 minutes, resulting in the initial UV-Vis-NIR spectral acquisition beginning approximately 3-4 minutes after the CO purge.

ESI-MS spectra were tested on a Bruker Impact II ESI-MS system (Bruker, Germany) under negative ion mode. The resulting precipitate was then dissolved in deionized water until completely dissolved, and the resulting solution was measured.

Photoluminescence spectroscopy was performed with a F7000 (Hitachi, Japan) spectrophotometer at room temperature, the voltage of the photomultiplier tube is 600 V, the width of both slits is 5 nm.

Temperature-dependent PL spectra of the clusters were recorded using a B&W TEK Exemplar Plus BTC655N spectrophotometer.

Calculated Details:

All geometry optimizations of Au nanoclusters were performed using the ORCA program package,[S2] employing density functional theory (DFT).[S3] The hybrid Becke three-parameter Lee-Yang-Parr (B3LYP) functional[S4] and the Perdew-Burke-Ernzerhof (PBE) functional[S5] were used for structural optimization and property calculations. A def2-TZVP triple-ζ basis set augmented with polarization functions was used for all atoms.[S6] To improve computational efficiency, the resolution-of-identity (RIJ)[S7] approximation was employed using the corresponding auxiliary basis set. Long-range dispersion interactions were accounted for using Grimme's empirical dispersion correction with Becke-Johnson damping (D3BJ).[S8] This correction provides a more accurate description of van der Waals interactions, which are crucial for the stability and properties of metallic nanoclusters. The optimized structure, confirmed to be at a local energy minimum by frequency analysis, served as the basis for further calculations.

Optical absorption spectrum was generated using the super-fast approximate time-dependent density functional theory (TD-DFT) approach,[S9] as implemented in ORCA by Grimme et al.

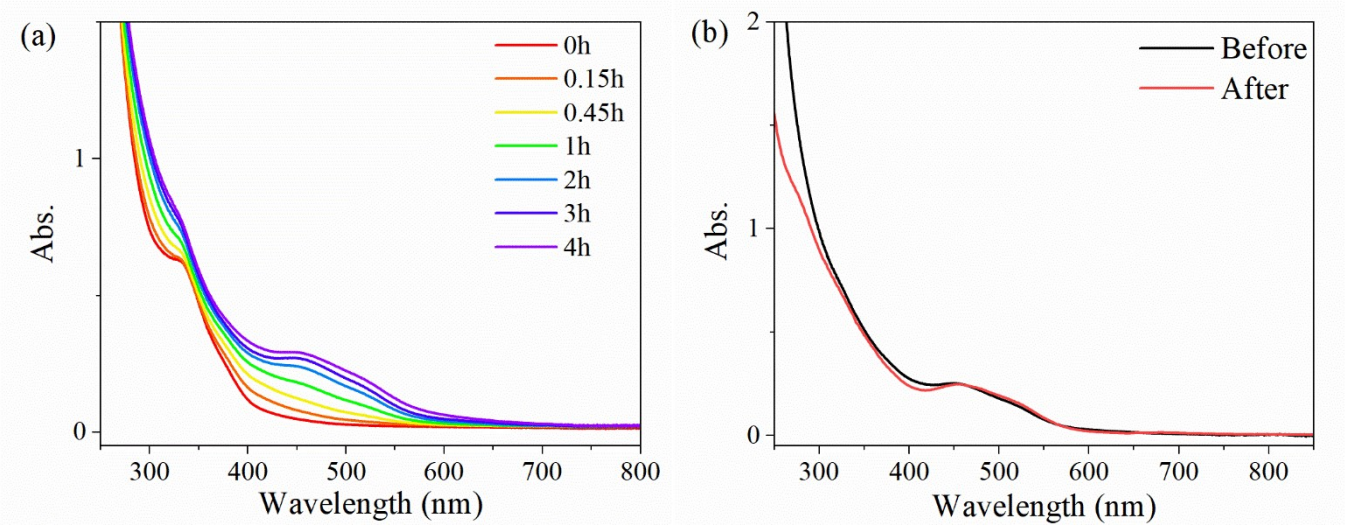

Figure S1. (a) Time-dependent UV-vis-NIR absorption spectra of the reaction solution during the synthesis of $Au_{21}Cys_{17}$, (b) the UV-vis-NIR absorption spectra of $Au_{21}Cys_{17}$ before and after purification.

The absorption spectra in Figure S1a reveal the dynamic process of the synthesis of $Au_{21}Cys_{17}$. Based on the spectral profile, the addition of reducing agent ($NaBH_4$) triggered an immediate emergence of a distinct absorption peak at 340 nm. However, this characteristic peak became progressively obscured due to increasing background absorption across the 300-400 nm range as the reaction proceeded. Notably, around the one-hour mark, two new absorption features developed at 455 nm and 515 nm, both exhibiting steady intensity enhancement with extended reaction time. Crucially, beyond the three-hour mark, substantial baseline elevation throughout the 400-600 nm region diminished the spectral resolution of these key absorption peaks. This spectral degradation profile prompted termination of the reaction at the optimized three-hour timepoint to preserve critical spectral features while maximizing target signal development.

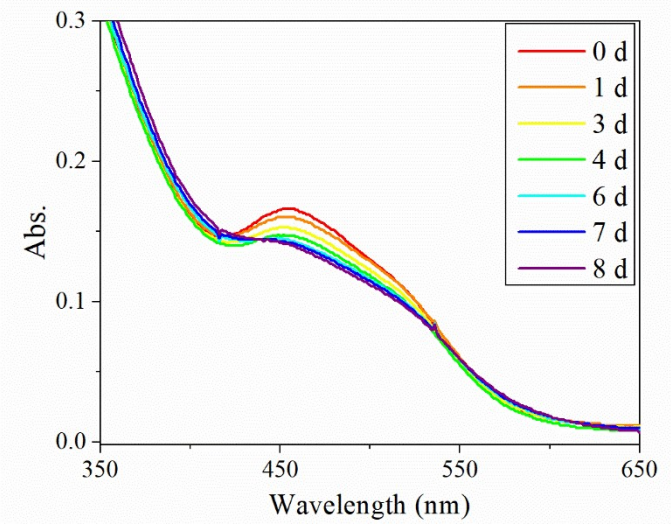

Figure S2. Time-dependent UV-vis absorption spectra of the aqueous solution of $Au_{21}Cys_{17}$ storing at 4 °C.

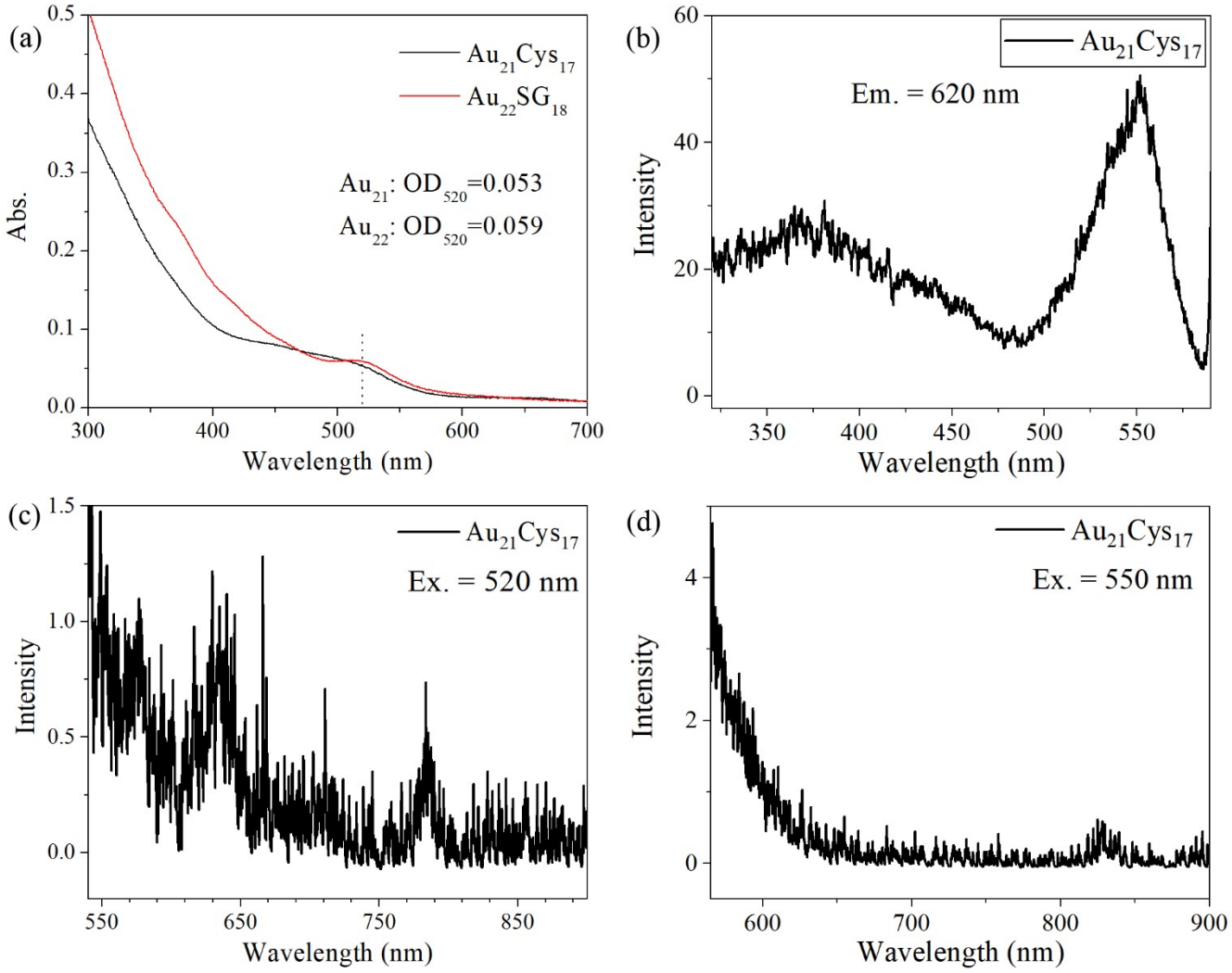

Figure S3. (a) UV-vis absorption of $Au_{21}Cys_{17}$ and $Au_{22}SG_{18}$ nanocluster in aqueous solutions, (b) excitation spectrum of $Au_{21}Cys_{17}$ in R_{gylc}=70% gylcerol/water solution (Em is 620 nm), and emission spectra of the $Au_{21}Cys_{17}$ in aqueous solutions excited by (c) 520 nm and (d) 550 nm.

As shown in Figure 5 in the main text, $Au_{21}Cys_{17}$ exhibits emission in the range of 550–650 nm, with a peak around 590 nm. The excitation spectrum (Figure S3b) shown an excitation peak at 550 nm when emission is 620 nm. However, excited by 520 nm, the emission spectrum of $Au_{21}Cys_{17}$ in pure aqueous solution (Figure S3c) reveals that the intensity between 580–610 nm, a region close to the expected peak, is actually lower than that of the adjacent spectral regions. This indicates the absence of a distinct emission peak in this range. Furthermore, when compared to the noise level observed in the 800–900 nm region, the signal in the 580–610 nm range does not exceed three times the signal-to-noise ratio. Excited by 550nm, there is no obvious emission peak within this range (Figure S3d). Therefore, it can be concluded that $Au_{21}Cys_{17}$ in aqueous solution does not exhibit detectable fluorescence.

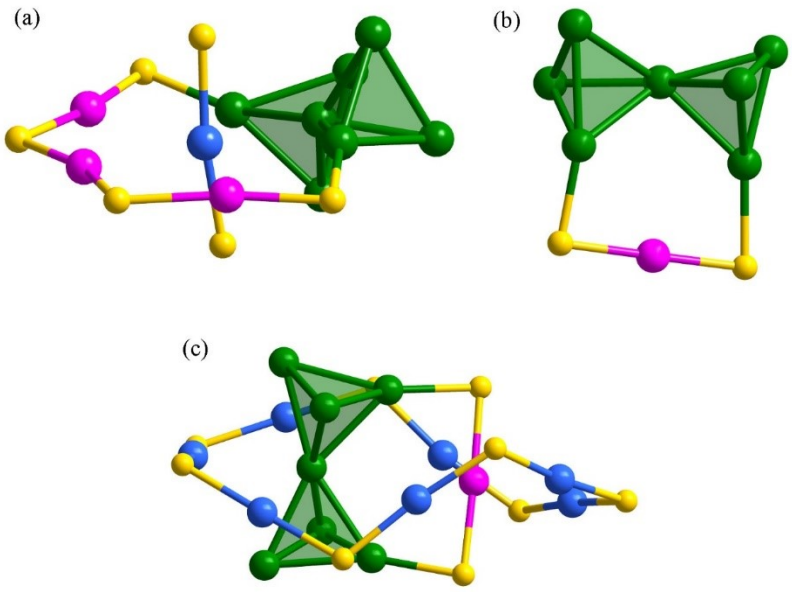

Figure S4. (a) Au_6 loop module with central Au(I) atom, (b) Au_4 loop modules in $Au_{20}SR_{16}$ NCs, and (c) the ring-in-ring structure in $Au_{21}SR_{17}$ nanocluster. Color labels: green, magenta, and light blue, Au; yellow, S.

In both $Au_{20}SR_{16}$ and $Au_{22}SR_{18}$, the ring staple thread through Au_6 loops formed by the Au_3SR_4 staple and three core Au atoms, forming an interlocked, catenane-like architecture. Moreover, due to aurophilic interactions, one Au(I) atom within the circular staple is positioned at the center of the Au_6 loop. In $Au_{21}SR_{17}$, the Au_7S_7 ring similarly threads through two such Au_6 loops. However, it cannot fully circumvent the Au_4 loop associated with the $AuSR_2$ staple (as the Au_8S_8 in $Au_{20}SR_{16}$), nor is it fully interlocked ("catenated") with three Au6 loops like the Au6S6 staple ring in $Au_{22}SR_{18}$.

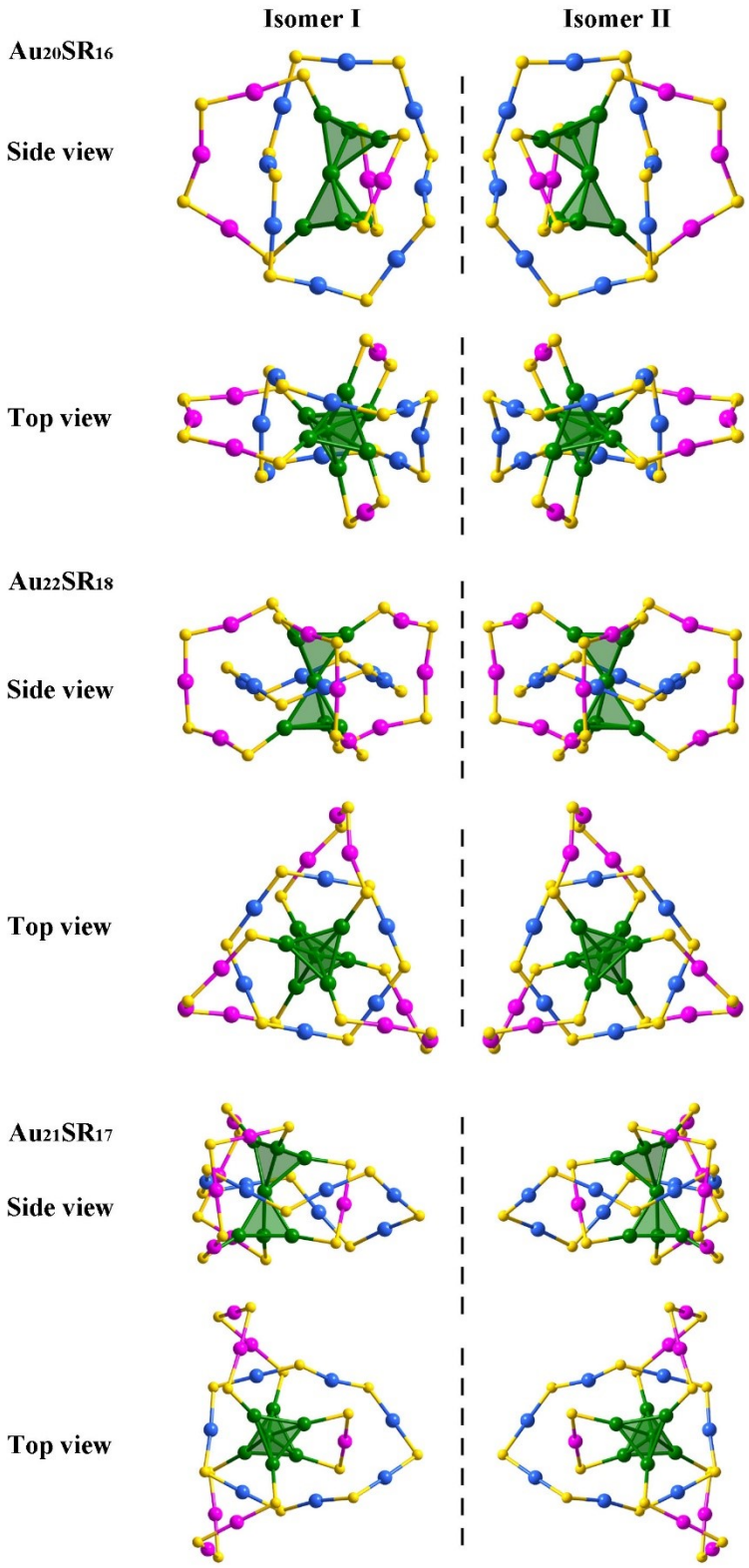

Figure S5. Isomer structures of three $4e^-$ Au NCs in side and top views. Color labels: green, magenta, and light blue, Au; yellow, S. Organic ligands omitted for clarity.

Building upon structural insights in Figure S, it is noteworthy that certain atomically precise gold nanoclusters are known to exhibit chirality. The $Au_{20}SR_{16}$ nanocluster has been characterized as possessing a

pair of enantiomers. Similarly, in the case of $Au_{22}SR_{18}$, its chiral nature arises from the distinct bonding configurations of three Au_3SR_4 staple motifs around a central Au_7 core. These different 'positions' or orientations of the staple units lead to the formation of a pair of enantiomeric structures. Based on this established structural precedent, we can reasonably predict that $Au_{21}SR_{17}$ would also exhibit chirality, potentially existing as a pair of enantiomers. Our theoretical calculations and structural modeling, as visualized in Figure S5, support this prediction, indicating analogous geometric arrangements that would give rise to enantiomeric forms of this specific cluster composition.

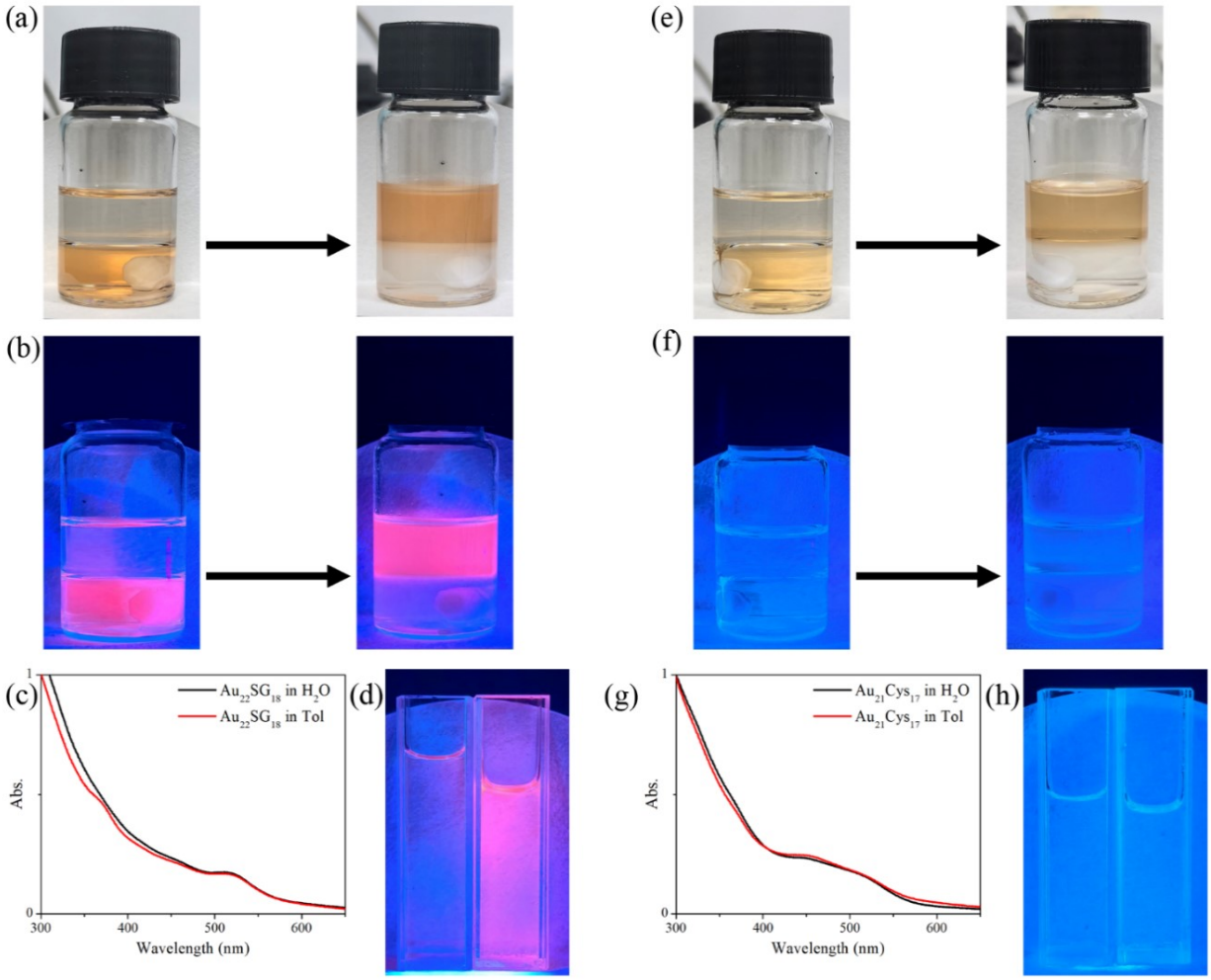

Figure S6. The photographs of $Au_{22}SG_{18}$ solution before and after phase transferring from water to toluene under natural light (a) and UV light (b), (c) the UV-vis absorption spectra and (d) photograph of $Au_{22}SG_{18}$ in water and toluene, the photographs of $Au_{21}Cys_{17}$ solution before and after phase transferring from water to toluene under natural light (e) and UV light (f), (g) the UV-vis absorption spectra and (h) photograph of $Au_{21}Cys_{17}$ in water and toluene.

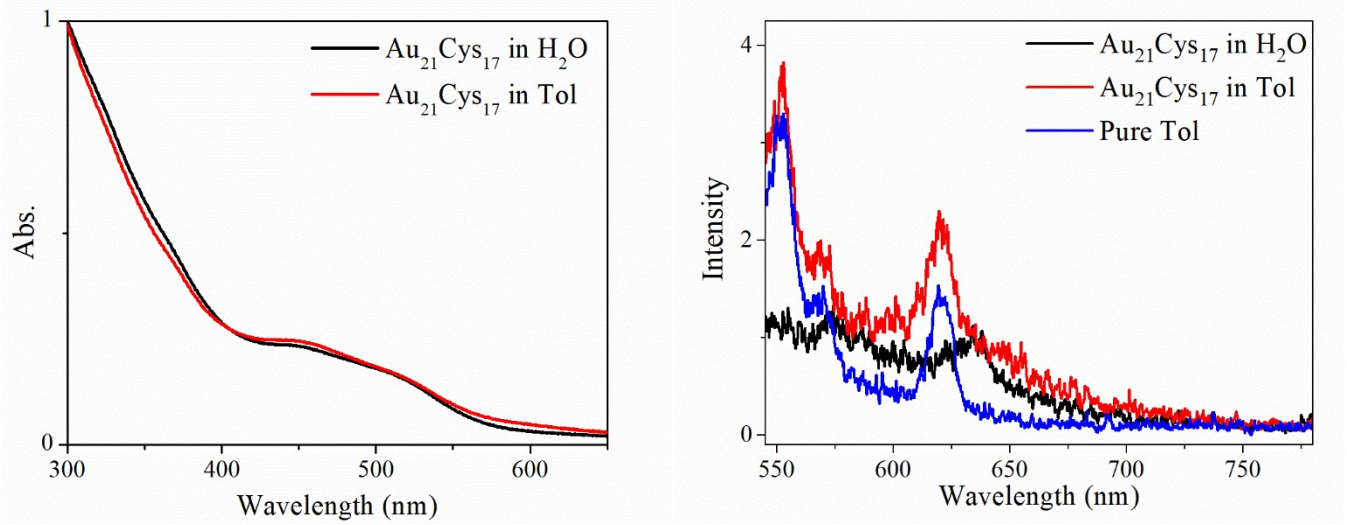

Figure S7. UV-vis absorption (left) and emission spectra (right) of $Au_{21}Cys_{17}$ dissolved in water (black line) and toluene (red line), and emission spectrum of pure toluene (blue line), all of these emission spectra are excited by 520 nm light.

Figure S6 demonstrates that both $Au_{21}Cys_{17}$ and $Au_{22}SG_{18}$ exhibit no discernible color change and maintain unaltered absorption spectra before and after the phase transfer. This indicates that our method is effective for transferring $Au_{21}Cys_{17}$ and $Au_{22}SG_{18}$ into toluene solutions from water. Notably, upon transfer from aqueous to toluene phases, $Au_{22}SG_{18}$ shows a significant enhancement in fluorescence, as depicted in Figure S6d. The photograph, comparing an aqueous solution of $Au_{22}SG_{18}$ (left) with its toluene solution (right), clearly reveals a much brighter fluorescence in the toluene phase. In contrast, as shown in Figure S6h, neither the aqueous nor the toluene solutions of $Au_{21}Cys_{17}$ displayed any significant fluorescence before or after the phase transfer.

A similar conclusion can be drawn from Figure S7: even when the absorbance values of the aqueous and toluene solutions are comparable, the photoluminescence intensity of the toluene solution does not exceed that of the aqueous solution after correcting for the intrinsic luminescence of the solvent—despite a slight apparent increase in photoluminescence in toluene.

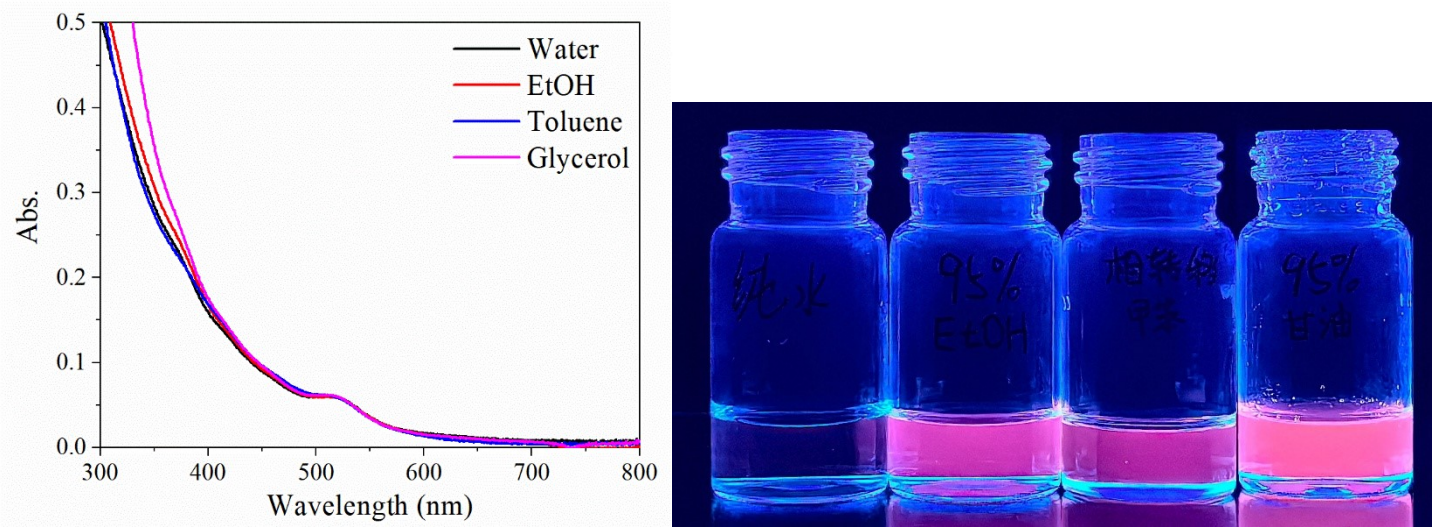

Figure S8. UV-vis absorption spectra and photograph of the $Au_{22}SG_{18}$ nanocluster in various solvents (left to right: water, 95% EtOH, toluene and 95% Glycerol).

The photograph (Figure S8) reveals a nearly imperceptible fluorescence response from the $Au_{22}SG_{18}$ aqueous solution. In contrast, the dispersion in 95% ethanol demonstrates a visibly higher brightness compared to the toluene dispersion. This enhancement in luminescence within the ethanol medium could stem from increased light scattering, potentially driven by the aggregation of clusters into larger nanoparticle structures. Intriguingly, the fluorescence intensity in 95% glycerol is considerably elevated over that in the 95% ethanol dispersion, even in the absence of any apparent cluster aggregation in glycerol.

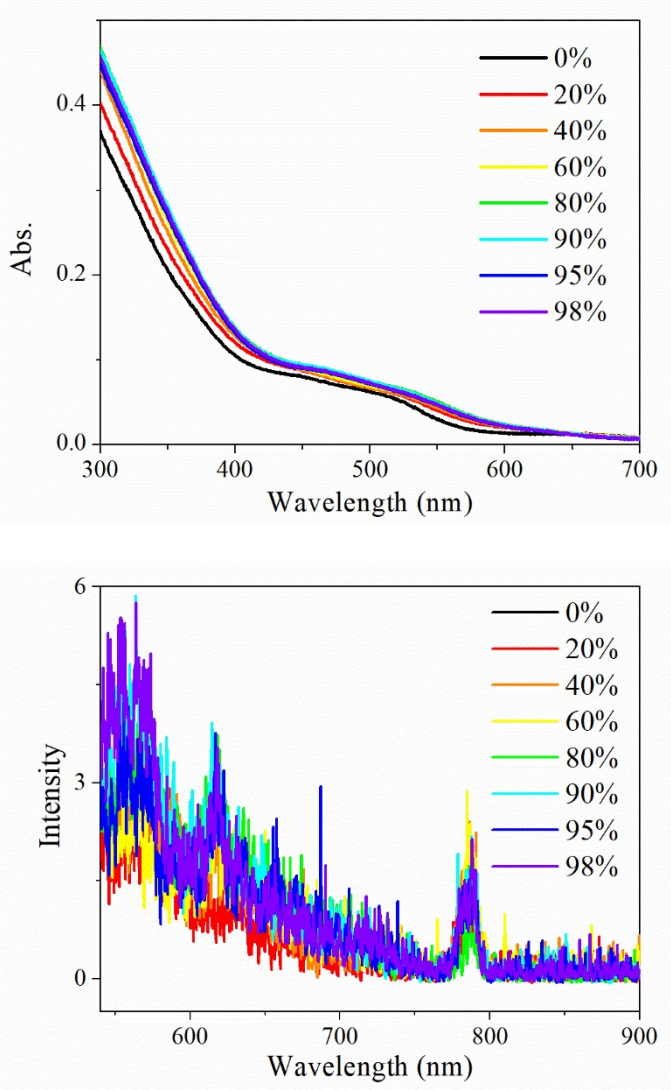

Figure S9. UV-vis absorption, and emission spectra of $Au_{21}Cys_{17}$ in various f_e ($f_e = v_{(EtOH)}/v_{(EtOH+H2O)}$) excited by 520 nm light.

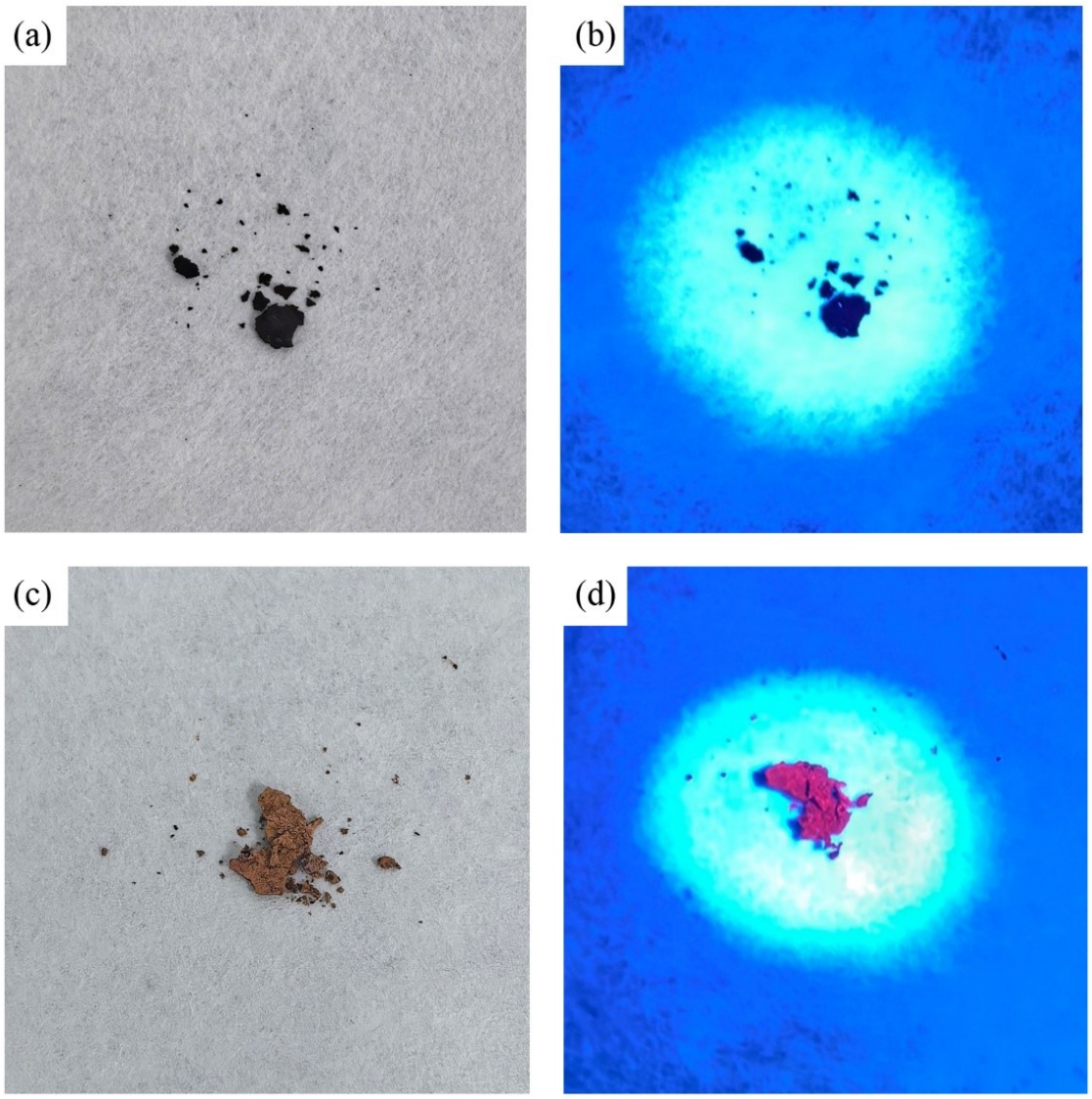

Figure S10. The photographs of $Au_{21}Cys_{17}$ powders under (a) natural light and (b) UV light irradiation, and the photographs of $Au_{22}SG_{18}$ powders under (c) natural light and (d) UV light irradiation.

From Figure S10, it is evident that the $Au_{22}SG_{18}$ solid powder exhibits pronounced fluorescence emission properties under UV light irradiation, demonstrating a distinct aggregation-induced emission (AIE) phenomenon. The observed robust fluorescence in $Au_{22}SG_{18}$ solid powder indicates effective restriction of intramolecular vibrational motions, thereby promoting radiative transitions and subsequent fluorescence emission. Conversely, under identical experimental conditions, $Au_{21}Cys_{17}$ solid powder displays negligible fluorescence. This stark contrast reveals that despite vibrational restriction, no fluorescence enhancement occurs in this system, conclusively demonstrating the absence of inherent fluorescence emission characteristics in $Au_{21}Cys_{17}$.

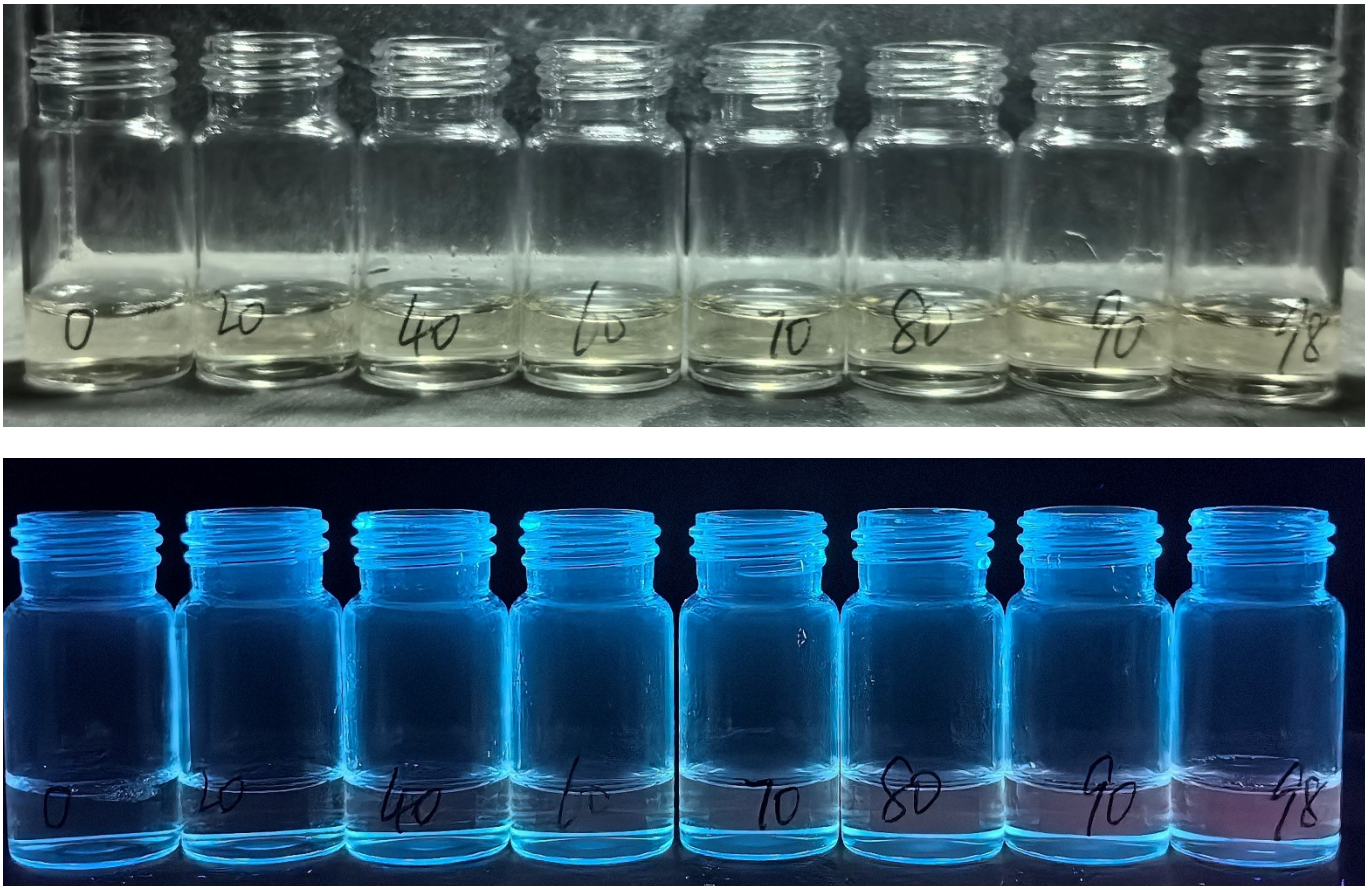

Figure S11. photograph of the $Au_{21}Cys_{17}$ nanocluster in glycerol/water solutions of varying concentrations (lables on the vases is the volume ratio of glycerol).

Figure S12. photograph of the $Au_{22}SG_{18}$ nanocluster in glycerol/water solutions of varying concentrations (lables on the vases is the valume ratio of glycerol).

Table S1 The transitions corresponding to the 515 nm peak of $Au_{21}(SCH_3)_{17}$ NC calculated according to TD-DFT method.

Number	Transition	Contribution	E (eV)/(nm)	Oscillator	λ_{exp} (nm)
1	HOMO→LUMO	99.5%	2.051/605	0.00100	---
2	HOMO→LUMO+1	99.3%	2.178/569	0.00540	515 nm
3	HOMO-1→LUMO HOMO-2→LUMO	70.5% 19.5%	2.278/545	0.00150	
4	HOMO-2→LUMO HOMO-1→LUMO+1 HOMO-1→LUMO	52.0% 22.2% 20.2%	2.301/537	0.00850	
5	HOMO-1→LUMO+1 HOMO-2→LUMO	69.1% 24.7%	2.394/518	0.04370	
6	HOMO-3→LUMO HOMO-2→LUMO+1 HOMO-4→LUMO	71.4% 14.5% 6.8%	2.443/508	0.00020	
7	HOMO-4→LUMO HOMO-2→LUMO+1 HOMO-3→LUMO	49.1% 23.0% 21.5%	2.473/501	0.00400	
8	HOMO-2→LUMO+1 HOMO-4→LUMO HOMO→LUMO+2	37.2% 35.5% 15.9%	2.493/497	0.00140	
9	HOMO→LUMO+2 HOMO-2→LUMO+1 HOMO-4→LUMO	79.9% 6.9% 6.1%	2.502/495	0.02210	
10	HOMO-5→LUMO HOMO-3→LUMO+1	81.4% 11.1%	2.571/482	0.00240	

Noted: Only MO transitions with absolute contribution ⩾5.0% are shown below.

Table S2 Energies of Kohn-Sham Orbitals for $Au_{21}(SCH_3)_{17}$.

Orbital Number	**Energy (eV)**	**Orbital Number**	**Energy (eV)**
LUMO+10	-1.59	HOMO-3	-5.151
LUMO+9	-1.696	HOMO-4	-5.169
LUMO+8	-1.785	HOMO-5	-5.272
LUMO+7	-1.876	HOMO-6	-5.359
LUMO+6	-1.921	HOMO-7	-5.426
LUMO+5	-1.963	HOMO-8	-5.487
LUMO+4	-2.087	HOMO-9	-5.499
LUMO+3	-2.191	HOMO-10	-5.526
LUMO+2	-2.33	HOMO-11	-5.541
LUMO+1	-2.623	HOMO-12	-5.555
LUMO	**-2.748**	HOMO-13	-5.606
HOMO	**-4.785**	HOMO-14	-5.631
HOMO-1	-4.952	HOMO-15	-5.76
HOMO-2	-4.993		

References:

[S1] Yu, Y., Luo, Z., Chevrier, D. M., Leong, D. T., Zhang, P., Jiang, D.-e., Xie, J., Identification of a highly luminescent $Au_{22}(SG)_{18}$ nanocluster. *J. Am. Chem. Soc.* **2014,** *136*, 1246-1249.

[S2] Neese, F., The ORCA program system. *WIREs Comput. Mol. Sci.* 2012, *2*, 73-78.

[S3] Becke, A. D., Density-functional thermochemistry. III. The role of exact exchange. *J. Chem. Phys.* 1993, *98*, 5648-5652.

[S4] Lee, C., Yang, W., Parr, R. G., Development of the Colle-Salvetti correlation-energy formula into a functional of the electron density. *Phys. Rev. B* 1988, *37*, 785-789.

[S5] Perdew, J. P., Burke, K., Ernzerhof, M., Generalized Gradient Approximation Made Simple. *Phys. Rev. Lett.* 1996, *77*, 3865-3868.

[S6] Weigend, F., Ahlrichs, R., Balanced basis sets of split valence, triple zeta valence and quadruple zeta valence quality for H to Rn: Design and assessment of accuracy. *Phys. Chem. Chem. Phys.* 2005, *7*, 3297-3305.

[S7] Neese, F., An improvement of the resolution of the identity approximation for the formation of the Coulomb matrix. *J. Comput. Chem.* 2003, *24*, 1740-1747.

[S8] Grimme, S., Ehrlich, S.; Goerigk, L., Effect of the damping function in dispersion corrected density functional theory. *J. Comput. Chem.* 2011, *32*, 1456-1465.

[S9] de Wergifosse, M., Grimme, S., Nonlinear-response properties in a simplified time dependent density functional theory (sTD-DFT) framework: Evaluation of the first hyperpolarizability. *J. Chem. Phys.* 2018, *149*, 024108.